Design of a Three-Axis Force Sensor Using Decoupled Compliant Parallel Mechanisms

Haiyang Li, *Member, IEEE*, Longteng Yi, Chuyang Leng, Yahan Zhong, Jiaqi Hong, Xueguan Song, and Guangbo Hao

***Abstract*— Multi-axis force sensors are integral to a wide range of high-tech applications, including robotics and machine monitoring. However, a significant challenge in their use is the high cross-axis coupling, which detrimentally affects measurement accuracy. To address this critical issue, this paper presents a comprehensive design method for multi-axis force sensors. This approach utilizes compliant parallel mechanisms, effectively decoupling the measured forces on multiple axes and enabling precise and independent measurement of each component force within the multi-axis system. Focusing on three-axis force sensors as a case study, this paper elucidates the proposed design principle. The comprehensive study covers system configuration, mechanical design, analytical modeling, numerical simulation, prototype development, and experimental evaluation. The resultant three-axis force sensor, prior to calibration, exhibits an average coupling error of just about 1.5%, underscoring its superior decoupling capability. The design concept and methodologies outlined here offer valuable insights for the development of self-decoupling multi-axis force sensors, advancing the field significantly.**

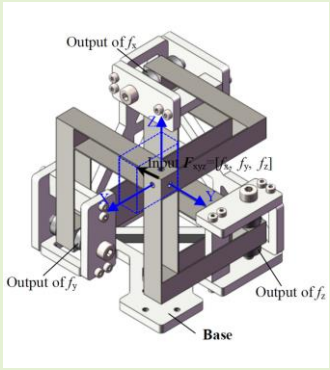

***Index Terms*—Three-axis force sensor, Compliant parallel mechanism, Cross-axis decoupling, Mechanism synthesis**

I. Introduction

MULTI-AXIS force sensors are essential components for sensing and providing feedback on force information along multiple axes. They possess the capability to simultaneously measure forces or torques in two or more directions within Cartesian coordinates. These sensors find applications across diverse fields, including robotics[1, 2, 3], biomedical applications [4, 5, 6], medical devices [7, 8], manufacturing [9], automotive [10, 11], aerospace [12], and beyond [13]. Given that force is an intensity property that cannot be directly measured [14], force sensors typically acquire external force information by assessing the deformation or displacement of the elastic-sensitive elements within them. Consequently, elastic-sensitive elements play a pivotal role in multi-axis force sensors, with their design significantly influencing key characteristics such as cross-axis coupling, measuring range and sensitivity [15].

Leveraging the principles of measuring the deformation or displacement of elastic-sensitive elements, multi-axis force sensors can be categorized into various types: resistive strain-type [16, 17, 18], piezoelectric-type [19, 20], capacitive-type [21], and optoelectronic-type [22, 23, 24, 25, 26]. Presently, the resistive strain-type of multi-axis force sensors is the most established and widely employed, thus this paper focuses on such type of multi-axis force sensors. In an ideal multi-axis force sensor, the signal value for each output channel should rely solely on the force or torque applied to that specific channel, remaining unaffected by forces or torques on other channels. However, factors such as the design of elastic-sensitive elements, precision of machining, strain gauge bonding techniques, lateral effects of strain gauges, and detection approaches may lead to forces or torques applied on different measurement channels influencing each other. This occurrence is commonly referred to as the cross-axis coupling in multi-axis force sensors.

Typically, a cross-axis coupling exceeding 5% significantly impacts the measurement quality of the multi-axis force sensor [27]. Hence, decoupling design is essential for multi-axis force sensors. The prevalent decoupling approaches for resistive strain-type multi-axis force sensors can be categorized into three main types: software decoupling, sensor layout decoupling, and hardware decoupling. Conventional software decoupling methods typically rely on the least squares approach to address the decoupling matrix. While this technique is conceptually straightforward and suitable for online decoupling, it necessitates matrix inversion, rendering it vulnerable to ill-conditioned matrices. Even minor disturbances in the experimental data can lead to notable changes in the

This work was supported by the National Natural Science Foundation of China under 51975108. *(Corresponding author: Haiyang Li.)*

Haiyang Li is with the School of Mechanical Engineering, Dalian University of Technology, Dalian 116024, China (e-mail: haiyang_li@dlut.edu.cn).

Longteng Yi is with the School of Mechanical Engineering, Dalian University of Technology, Dalian 116024, China.

Chuyang Leng is with the School of Mechanical Engineering, Dalian University of Technology, Dalian 116024, China.

Yahan Zhong is with the School of Mechanical Engineering, Dalian University of Technology, Dalian 116024, China.

Jiaqi Hong is with the School of Mechanics and Aerospace Engineering, Dalian University of Technology, Dalian 116024, China.

Xueguan Song is with the School of Mechanical Engineering, Dalian University of Technology, Dalian 116024, China.

Guangbo Hao is with School of Engineering-Electrical and Electronic Engineering, University College Cork, Cork T12 K8AF, Ireland.

decoupling accuracy [28]. The emergence of artificial intelligence has prompted the application of various efficient machine learning approaches to address coupling concerns [29, 30, 31, 32]. Nonetheless, the enhanced complexity of decoupling algorithms has somewhat influenced the response speed. While sensor layout decoupling can mitigate the coupling to a certain extent, it does not provide a fundamental solution to the coupling problem [11, 15, 33, 34, 35]. Recently, there has been a growing focus on hardware decoupling [36, 37, 38, 39, 40, 41, 42]. Some researchers have chosen compliant mechanisms to replace the traditional elastic-sensitive elements, resulting in reduced cross-axis coupling errors and improved sensitivity [14, 43].

The concept of compliant mechanisms, introduced by Midha in the 1990s [44], typically involves rigid modules and flexible hinges, which include notched hinges and flexible beams. These mechanisms utilize the deformation of flexible hinges to transmit motion and force [45]. With the evolution of compliant mechanisms, an increasing number of researchers are adopting a comprehensive approach involving these mechanisms to guide the design of elastic-sensitive elements in multi-axis force sensors, intending to enhance sensitivity and mitigate cross-axis coupling. For instance, Yang et al. devised position and force sensors based on bridge and parallelogram-shaped compliant mechanisms, optimizing their sensitivity [46]. Jiang et al. developed a dual-range force sensor using a composite quadrilateral compliant mechanism, demonstrating high sensitivity [47]. Nguyen and Kuo proposed a well-engineered spoked structure torque sensor, employing a novel slotted spoke-type to develop force-sensing arms with a high sensitivity of 1.65 mV/Nm [16]. Simultaneously, leveraging the advantages of no friction, no backlash, and high resolution in compliant mechanisms [48], Wang et al. introduced a novel dual-frame six-axis force sensor. The internal elastic part measures F_x, F_y, and T_z, while the external elastic part measures T_x, T_y, and F_z, effectively reducing the cross-axis coupling effects in multi-axis force sensors [49]. Matich et al. created a state-of-the-art force/torque sensor based on the Stewart-Gough platform, demonstrating significant linearity and coupling errors of less than 2.76% [50]. It is evident that multi-axis force sensors incorporating compliant mechanisms as elastic-sensitive elements offer advantages in reducing cross-axis coupling and enhancing sensitivity. However, multi-axis force sensors designed using this approach still face challenges relating to relatively high coupling errors and have not fundamentally addressed the trade-off between sensitivity and measuring range.

This paper presents a novel design concept for multi-axis force sensors through the incorporation of decoupled compliant parallel mechanisms. In this innovative design approach, the traditional elastic-sensitive element of a multi-axis force sensor is substituted with a decoupled compliant parallel mechanism, facilitating superior cross-axis decoupling. Furthermore, the measuring principle in the new concept is transformed, moving away from reliance on the deformation of the decoupled compliant parallel mechanism and towards the measurement of the forces transformed by the mechanism. This shift in the measuring principle not only minimizes cross-axis coupling but also mitigates the limitations on the measuring range, thus alleviating the mutual constraint between cross-axis coupling and measuring range. Consequently, the new measuring principle circumvents the trade-offs, enabling enhancements in both cross-axis coupling and measuring ranges. This paper exemplifies the proposed concept through the design of a three-axis force sensor, with the following key contributions:

- Introduction of a new design concept for multi-axis force sensors, utilizing self-decoupling compliant parallel mechanisms to achieve enhanced cross-axis decoupling. Additionally, the new measuring principle also reduces the coupling between sensitivity and measuring range.
- Proposition of a three-axis force sensor, accompanied by the synthesis, modeling, and experimental testing of the associated XYZ compliant parallel mechanism.

The remaining sections of this paper are organized as follows: Section II introduces the design approach of a multi-axis compliant parallel mechanism with self-decoupling functionality. It provides a detailed overview of a design synthesis approach for an XYZ compliant parallel mechanism based on constrained flow, resulting in multiple sets of elastic-sensitive structures with XYZ decoupling functionality. In Section III, a specific compliant parallel mechanism is selected for analytical modeling and finite element simulation to obtain the input-output characteristics of the compliant parallel mechanism and validate its decoupling performance. Section IV describes the system composition of the three-axis force sensor and presents the fabrication of a prototype for performance testing. Finally, Section V summarizes the primary conclusions of this paper and provides insights into potential avenues for future research.

II. Design of Three-Axis Force Sensor

Based on the proposed design concept of multi-axis force sensors, a diagram of the three-axis force sensors is formed as shown in Fig. 1. The topological structure of the decoupled XYZ compliant parallel mechanisms is depicted on the right side of the Fig. 1. It includes three types of rigid modules: input rigid module (IRM), output module (ORM), and fixed module (FRM), along with two types of compliant modules: decoupling compliant module (DCM) and guiding compliant module (GCM). The measured three-axis resultant forces are applied to the IRM. The three DCMs (X-DCM, Y-DCM, and Z-DCM) facilitate the decomposition of the three-axis resultant force into three component forces and subsequently transmit these component forces to the three ORMs (X-ORM, Y-ORM, and Z-ORM). Meanwhile, the GCMs (X-GCM, Y-GCM, and Z-GCM) guide the ORMs to move along the directions of the component forces, respectively. The component forces transmitted by the three ORMs can be measured using three single-axis force sensors, such as piezoelectric ceramic single-axis force sensors. The outputs of these three single-axis force sensors collectively form the outputs of the three-axis force sensor. The diagram of the three-axis force sensor signal processing system is depicted on the left side of Fig. 1. The measured single-axis force signals are transmitted to the micro-processor through processes such as signal conditioning and signal processing. Ultimately, decoupled three-axis force values are obtained, enabling measurement of three-axis forces. It can be observed that the design of the compliant parallel mechanisms with self-decoupling is the key compared with the traditional three-axis force sensors. Therefore, this section

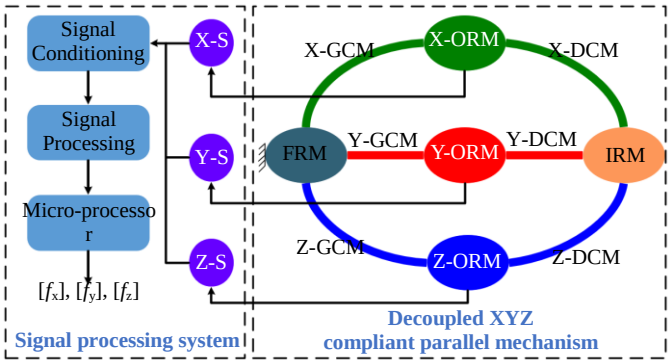

Fig. 1. Topological structure of the three-axis force sensor: XYZ compliant parallel mechanism and signal processing system (Rigid modules are represented by elliptical shapes, while compliant modules GCM and DCM are denoted by bold arches. The input force is applied to IRM and is indicated by an orange arrow. Pressure sensors X-S, Y-S and Z-S are shown in purple circles, measure the contact with measurement modules X-ORM, Y-ORM, and Z-ORM, enabling the collection of individual force components).

TABLE I
DEGREES OF FREEDOM OF THE RIGID MODULES

Rigid modules	X	Y	Z	θ_X	θ_Y	θ_Z
IRM	Yes	Yes	Yes	No	No	No
X-ORM	Yes	No	No	No	No	No
Y-ORM	No	Yes	No	No	No	No
Z-ORM	No	No	Yes	No	No	No
FRM	No	No	No	No	No	No

focuses on the design, especially the synthesis, of the associated XYZ compliant parallel mechanisms with self-decoupling characteristics (or decoupled XYZ compliant parallel mechanisms).

The design of decoupled XYZ compliant parallel mechanisms presents myriad challenges, particularly in the synthesis process, which must consider various factors such as cross-axis motion and actuation decoupling, actuation isolation, compactness, dynamic performance, lightweight construction, and compatibility with diverse manufacturing processes [51, 52, 53, 54, 55]. Numerous studies have focused on synthesizing decoupled XYZ compliant parallel mechanisms, resulting in a spectrum of design approaches. Notably, the rigid-body replacement method [56, 57], freedom, actuation, and constraint topologies (FACT) method [58, 59], topology optimization-based approach [60, 61, 62, 63, 64, 65], constraint and position identification (CPI) approach [66], and constraint-flow based method [67] have contributed to the production of multiple design alternatives. Among these approaches, the constraint-flow based method has demonstrated effectiveness in identifying all constraints of associated compliant modules to meet design requirements, albeit its current application is limited to XYθ compliant parallel mechanisms mainly for the applications of motion platforms [67]. Therefore, this paper focuses on the synthesis of decoupled XYZ compliant parallel mechanisms utilizing the constraint-flow based method for the application of three-axis force sensors.

The design process, as depicted in Fig. 2, involves several crucial steps, as shown below:

Step 1: Determine the topology of compliant mechanism. With the design objective of creating a three-axis force sensor with self-decoupling capabilities, the required mechanism to be

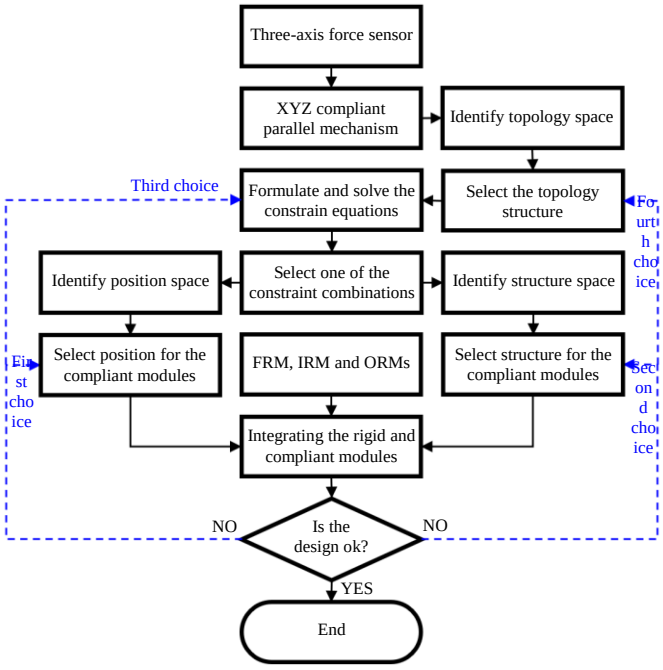

Fig. 2. A method for synthesizing a decoupled XYZ compliant parallel mechanism.

designed is determined as the XYZ compliant parallel mechanism. Select the topology of the compliant mechanism based on constraint chain configurations and sensor layout strategies. For the same type of compliant mechanism, there exist multiple design options for constraint chain configuration. For example, designs may involve two compliant modules and one rigid module, as depicted in Fig. 1, or they may feature three compliant modules and two rigid modules. Therefore, the topology of the decoupled XYZ compliant parallel mechanism is not unique. All possible topologies form a topology space. This paper employs the topology structure depicted in Fig. 1 for configuration synthesis.

Step 2: Formulate and solve the constraint equations to obtain the desired constraint combinations that meet the specified requirements. According to the motion requirements of the rigid modules, the constraint equations for the compliant modules are derived. These equations consist of two parts: constraint equilibrium equations and initial constraint conditions. The former describes the mutual constraints among modules within the mechanism, which is characterized by the equivalence of the constraints in the rigid modules to those originating from the base and subsequently modulated through the compliant modules, as illustrated in Fig. 3. The latter specifies the specific requirements that the compliant mechanism must satisfy. By substituting the initial constraint conditions and solving the constraint equilibrium equations, permissible constraint combinations that meet the requirements are obtained.

Step 3: Based on the given permissible constraints, determine the structure of the compliant modules. Utilizing the design methods emphasized in the preceding text, we can obtain the permissible structures for the compliant modules. Given the constraints, the compliant modules can manifest various structural forms, as depicted in Fig. 4, thereby forming a structural space. Within this space, the desired structure for the

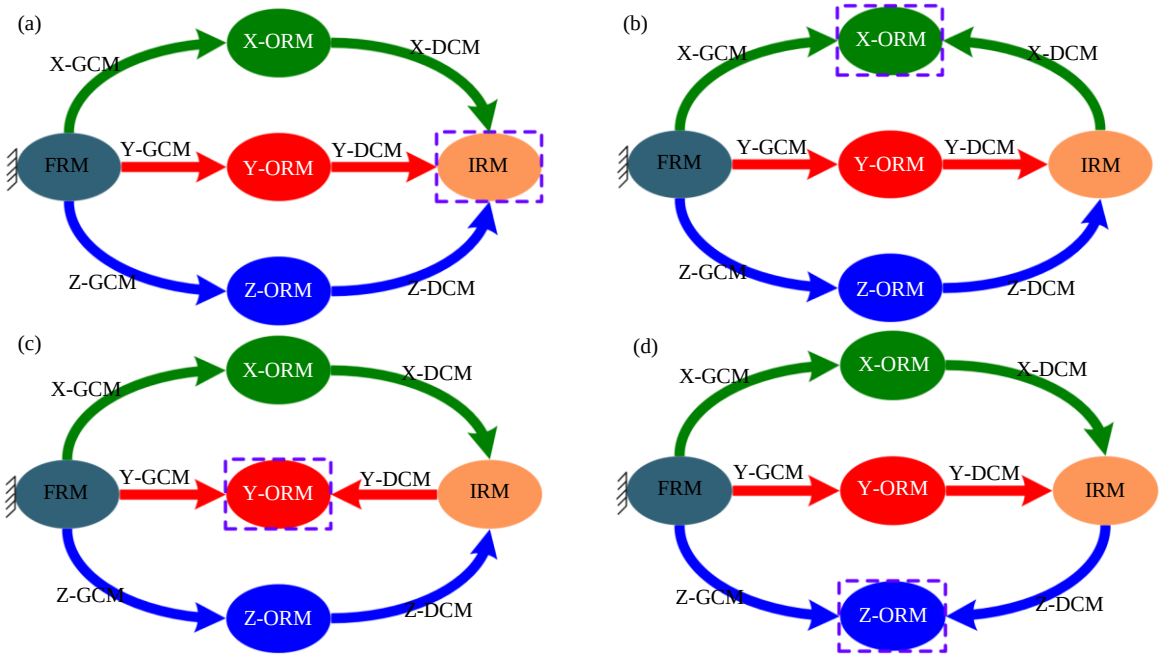

Fig. 3 Constraints transmitted from the ground to each rigid module: (a) Constraints transmitted from the ground to IRM, (b) Constraints transmitted from the ground to X-ORM, (c) Constraints transmitted from the ground to Y-ORM, and (d) Constraints transmitted from the ground to Z-ORM.

TABLE II
INITIAL VALUES OF THE CONSTRAINTS ON THE COMPLIANT MODULES.

Compliant modules	u	v	w	α	β	γ
$\mathscr{L}_{\text{X-GCM}}$	$u_{\text{x-gcm}}=0$	$v_{\text{x-gcm}}$	$w_{\text{x-gcm}}$	$\alpha_{\text{x-gcm}}$	$\beta_{\text{x-gcm}}$	$\gamma_{\text{x-gcm}}$
$\mathscr{L}_{\text{X-DCM}}$	$u_{\text{x-dcm}}$	$v_{\text{x-dcm}}=0$	$w_{\text{x-dcm}}=0$	$\alpha_{\text{x-dcm}}$	$\beta_{\text{x-dcm}}$	$\gamma_{\text{x-dcm}}$
$\mathscr{L}_{\text{Y-GCM}}$	$u_{\text{y-gcm}}$	$v_{\text{y-gcm}}=0$	$w_{\text{y-gcm}}$	$\alpha_{\text{y-gcm}}$	$\beta_{\text{y-gcm}}$	$\gamma_{\text{y-gcm}}$
$\mathscr{L}_{\text{Y-DCM}}$	$u_{\text{y-dcm}}=0$	$v_{\text{y-dcm}}$	$w_{\text{y-dcm}}=0$	$\alpha_{\text{y-dcm}}$	$\beta_{\text{y-dcm}}$	$\gamma_{\text{y-dcm}}$
$\mathscr{L}_{\text{Z-GCM}}$	$u_{\text{z-gcm}}$	$v_{\text{z-gcm}}$	$w_{\text{z-gcm}}=0$	$\alpha_{\text{z-gcm}}$	$\beta_{\text{z-gcm}}$	$\gamma_{\text{z-gcm}}$
$\mathscr{L}_{\text{Z-DCM}}$	$u_{\text{z-dcm}}=0$	$v_{\text{z-dcm}}=0$	$w_{\text{z-dcm}}$	$\alpha_{\text{z-dcm}}$	$\beta_{\text{z-dcm}}$	$\gamma_{\text{z-dcm}}$

compliant modules can be selected as needed.

Step 4: Going ahead with the design of the rigid modules. This design stage primarily focuses on determining the number of rigid modules, their topological positions, and the mechanical interfaces required for the sensors.

Step 5: Determine the specific positioning of the compliant modules. The spatial orientation of the compliant modules can be determined by the solutions of the constraint equations, but the specific positions are not defined. The set of multiple feasible locations constitutes the position space. Factors like manufacturability, spatial efficiency, and aesthetic appeal guide the final positioning of these modules.

Step 6: Synthesize the overall structure. Based on the determined number, structure, and positioning of the rigid and compliant modules, integrate them on the basis of the topological structure to obtain the desired XYZ compliant parallel decoupling mechanism, as illustrated in Fig. 5.

Step 7: Validate the design to ensure compliance with the design requirements. If the design fails to meet the specified evaluation criteria, the following approaches can be employed for redesign: (a) Select alternative compliant module positioning schemes from the position space in step 5 that meet the requirements; (b) Choose different permissible compliant module structures in step 3; (c) Select the remaining solutions of the constraint equations in step 2 to obtain new compliant constraint combinations that meet the requirements; (d) Choose new topological constraint schemes from the constraint space in step 1 and redesign the topological structure.

Based on the movement characteristics of the aforementioned rigid modules, their motilities are outlined in Table I. The degrees of freedom for the rigid modules depend on the constraints applied to them, and all constraints originate from the ground. For instance, the constraints applied to the FRM directly originate from the ground, as the FRM is directly fixed to the ground. On the other hand, the constraints applied to the IRM are indirectly transmitted through three flexible linkages, and these constraints are transmitted to different rigid modules through different paths, forming multiple constraint flows. The constraint transmissions related to the IRM, X-ORM, Y-ORM, and Z-ORM are illustrated in Fig. 3.

The constraints for the compliant modules and rigid modules are defined as vector $\mathscr{L}$ represented as in (1).

$$\mathscr{L} = \{\, u, v, w, \alpha, \beta, \gamma \,\}^{\mathrm{T}} \tag{1}$$

where u, v, w, α, β, and γ represent the stiffness of movement and rotation along the X, Y, and Z axes for compliant modules or the degrees of freedom for rigid modules. In this paper, each element in vector $\mathscr{L}$ has two forms: "0" and "1". "0" indicates relatively small stiffness, representing freedom, while "1" indicates relatively large stiffness, representing constraint.

It can be observed from Fig. 3 that the constraint transmission in this paper employs both series and parallel connections. Series connections are represented by the symbol "∩", while parallel connections are denoted by the symbol "∪", and their operational rules are defined by (2) and (3) [67].

$$\begin{aligned}\mathscr{L}_{\mathrm{a}} \cap \mathscr{L}_{\mathrm{b}} &= \{u_{\mathrm{a}}, v_{\mathrm{a}}, w_{\mathrm{a}}, \alpha_{\mathrm{a}}, \beta_{\mathrm{a}}, \gamma_{\mathrm{a}}\}^{\mathrm{T}} \cap \{u_{\mathrm{b}}, v_{\mathrm{b}}, w_{\mathrm{b}}, \alpha_{\mathrm{b}}, \beta_{\mathrm{b}}, \gamma_{\mathrm{b}}\}^{\mathrm{T}} \\ &= \{u_{\mathrm{a}} \times u_{\mathrm{b}}, v_{\mathrm{a}} \times v_{\mathrm{b}}, w_{\mathrm{a}} \times w_{\mathrm{b}}, \\ &\qquad \alpha_{\mathrm{a}} \times \alpha_{\mathrm{b}}, \beta_{\mathrm{a}} \times \beta_{\mathrm{b}}, \gamma_{\mathrm{a}} \times \gamma_{\mathrm{b}}\}^{\mathrm{T}}\end{aligned} \tag{2}$$

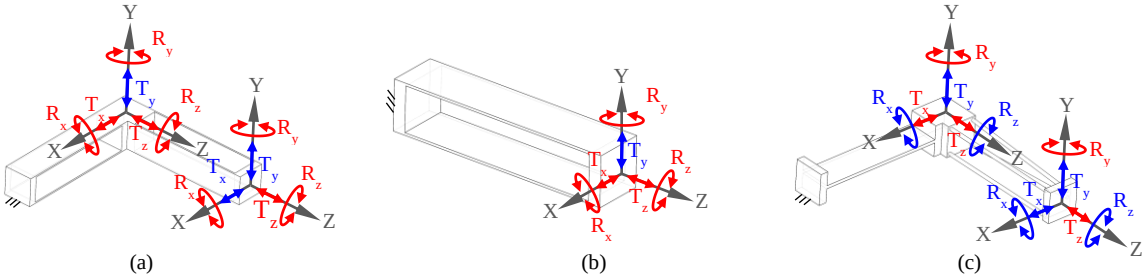

Fig. 4 Structures of the compliant modules: (a) X-GCM, Y-GCM, and Z-GCM in Case 1, (b) X-DCM, Y-DCM, and Z-DCM in Cases 1 and 2, (c) X-GCM, Y-GCM, and Z-GCM in Case 2 (T_x, T_y, T_z, R_x, R_y and R_z represent translations and rotations along/about the X, Y and Z-axes, and they are indicated by motion signs. The motion signs in red mean the associated motion is constrained, otherwise the motion is not constrained).

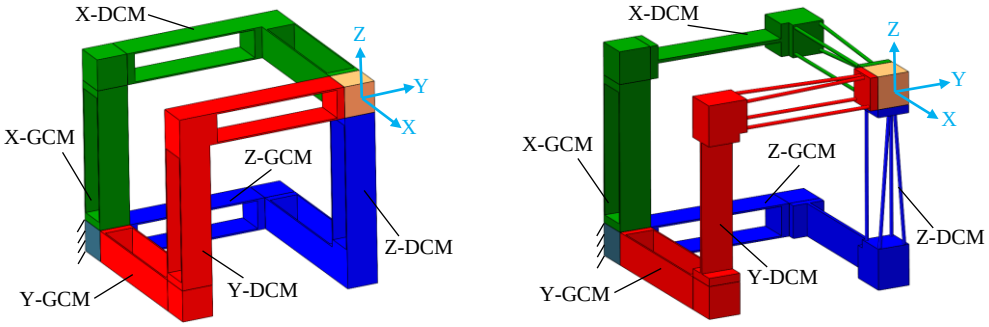

Fig. 5 Two asymmetric XYZ compliant parallel mechanisms: (a) Asymmetric design for Case-1, and (b) Asymmetric design for Case-2 (X-GCM and X-DCM are shown in green, Y-GCM and Y-DCM are shown in red, Z-GCM and Z-DCM are shown in blue, IRM is shown in orange, FRM is shown in grey).

$$\begin{aligned}\mathscr{L}_{\mathrm{a}} \cup \mathscr{L}_{\mathrm{b}} &= \{u_{\mathrm{a}}, v_{\mathrm{a}}, w_{\mathrm{a}}, \alpha_{\mathrm{a}}, \beta_{\mathrm{a}}, \gamma_{\mathrm{a}}\}^{\mathrm{T}} \cup \{u_{\mathrm{b}}, v_{\mathrm{b}}, w_{\mathrm{b}}, \alpha_{\mathrm{b}}, \beta_{\mathrm{b}}, \gamma_{\mathrm{b}}\}^{\mathrm{T}} \\ &= \{\phi[u_{\mathrm{a}}+u_{\mathrm{b}}], \phi[v_{\mathrm{a}}+v_{\mathrm{b}}], \phi[w_{\mathrm{a}}+w_{\mathrm{b}}], \\ &\quad \phi[\alpha_{\mathrm{a}}+\alpha_{\mathrm{b}}], \phi[\beta_{\mathrm{a}}+\beta_{\mathrm{b}}], \phi[\gamma_{\mathrm{a}}+\gamma_{\mathrm{b}}]\}^{\mathrm{T}}\end{aligned} \tag{3}$$

In (3), the function $\phi(x)$ is defined as shown in (4).

$$\phi(x) = \begin{cases} 0 & x = 0 \\ 1 & x \neq 0 \end{cases} \tag{4}$$

Based on the topological diagram in Fig. 1 and the above definitions, let the constraints for the GCM and DCM compliant modules be denoted as $\mathscr{L}_{\text{X-GCM}}$, $\mathscr{L}_{\text{X-DCM}}$, $\mathscr{L}_{\text{Y-GCM}}$, $\mathscr{L}_{\text{Y-DCM}}$, $\mathscr{L}_{\text{Z-GCM}}$, and $\mathscr{L}_{\text{Z-DCM}}$ as shown in (5) [67].

$$\begin{cases} \mathscr{L}_{\text{X-GCM}} = \{u_{\text{x-gcm}}, v_{\text{x-gcm}}, w_{\text{x-gcm}}, \alpha_{\text{x-gcm}}, \beta_{\text{x-gcm}}, \gamma_{\text{x-gcm}}\}^{\mathrm{T}} \\ \mathscr{L}_{\text{X-DCM}} = \{u_{\text{x-dcm}}, v_{\text{x-dcm}}, w_{\text{x-dcm}}, \alpha_{\text{x-dcm}}, \beta_{\text{x-dcm}}, \gamma_{\text{x-dcm}}\}^{\mathrm{T}} \\ \mathscr{L}_{\text{Y-GCM}} = \{u_{\text{y-gcm}}, v_{\text{y-gcm}}, w_{\text{y-gcm}}, \alpha_{\text{y-gcm}}, \beta_{\text{y-gcm}}, \gamma_{\text{y-gcm}}\}^{\mathrm{T}} \\ \mathscr{L}_{\text{Y-DCM}} = \{u_{\text{y-dcm}}, v_{\text{y-dcm}}, w_{\text{y-dcm}}, \alpha_{\text{y-dcm}}, \beta_{\text{y-dcm}}, \gamma_{\text{y-dcm}}\}^{\mathrm{T}} \\ \mathscr{L}_{\text{Z-GCM}} = \{u_{\text{z-gcm}}, v_{\text{z-gcm}}, w_{\text{z-gcm}}, \alpha_{\text{z-gcm}}, \beta_{\text{z-gcm}}, \gamma_{\text{z-gcm}}\}^{\mathrm{T}} \\ \mathscr{L}_{\text{Z-DCM}} = \{u_{\text{z-dcm}}, v_{\text{z-dcm}}, w_{\text{z-dcm}}, \alpha_{\text{z-dcm}}, \beta_{\text{z-dcm}}, \gamma_{\text{z-dcm}}\}^{\mathrm{T}} \end{cases} \tag{5}$$

The relationship between the degrees of freedom for rigid modules and the constraints for the compliant modules can be derived from Fig. 3, as shown in (6) to (9).

$$\mathscr{L}_{\text{X-ORM}} = \mathscr{L}_{\text{X-GCM}} \cup \{[(\mathscr{L}_{\text{Y-GCM}} \cap \mathscr{L}_{\text{Y-DCM}}) \cup (\mathscr{L}_{\text{Z-GCM}} \cap \mathscr{L}_{\text{Z-DCM}})] \cap \mathscr{L}_{\text{X-DCM}}\} \tag{6}$$

$$\mathscr{L}_{\text{Y-ORM}} = \mathscr{L}_{\text{Y-GCM}} \cup \{[(\mathscr{L}_{\text{X-GCM}} \cap \mathscr{L}_{\text{X-DCM}}) \cup (\mathscr{L}_{\text{Z-GCM}} \cap \mathscr{L}_{\text{Z-DCM}})] \cap \mathscr{L}_{\text{Y-DCM}}\} \tag{7}$$

$$\mathscr{L}_{\text{Z-ORM}} = \mathscr{L}_{\text{Z-GCM}} \cup \{[(\mathscr{L}_{\text{X-GCM}} \cap \mathscr{L}_{\text{X-DCM}}) \cup (\mathscr{L}_{\text{Y-GCM}} \cap \mathscr{L}_{\text{Y-DCM}})] \cap \mathscr{L}_{\text{Z-DCM}}\} \tag{8}$$

$$\mathscr{L}_{\text{IRM}} = (\mathscr{L}_{\text{X-GCM}} \cap \mathscr{L}_{\text{X-DCM}}) \cup (\mathscr{L}_{\text{Y-GCM}} \cap \mathscr{L}_{\text{Y-DCM}}) \cup (\mathscr{L}_{\text{Z-GCM}} \cap \mathscr{L}_{\text{Z-DCM}}) \tag{9}$$

where $\mathscr{L}_{\text{X-ORM}}$, $\mathscr{L}_{\text{Y-ORM}}$, $\mathscr{L}_{\text{Z-ORM}}$, and $\mathscr{L}_{\text{IRM}}$ represent the desired constraints for the rigid modules X-ORM, Y-ORM, Z-ORM, and IRM, respectively. According to Table I, the numerical values for $\mathscr{L}_{\text{X-ORM}}$, $\mathscr{L}_{\text{Y-ORM}}$, $\mathscr{L}_{\text{Z-ORM}}$, and $\mathscr{L}_{\text{IRM}}$ can be obtained as shown in (10).

$$\begin{cases} \mathscr{L}_{\text{X-ORM}} = \{0, 1, 1, 1, 1, 1\}^{\mathrm{T}} \\ \mathscr{L}_{\text{Y-ORM}} = \{1, 0, 1, 1, 1, 1\}^{\mathrm{T}} \\ \mathscr{L}_{\text{Z-ORM}} = \{1, 1, 0, 1, 1, 1\}^{\mathrm{T}} \\ \mathscr{L}_{IRM} = \{0, 0, 0, 1, 1, 1\}^{\mathrm{T}} \end{cases} \tag{10}$$

From Fig. 3(a), it is evident that the flexible chain where the X-ORM is located should have degrees of freedom for translation along the X-axis. Therefore, it can be deduced that the X-GCM compliant module has freedom of translation along the X-axis. Additionally, considering the motion of the IRM, the X-DCM compliant module should have degrees of freedom for translation along the Y and Z axes. Similarly, we can deduce the initial freedom values for Y-GCM, Y-DCM, Z-GCM, and Z-DCM, as shown in Table II.

Substituting these initial values into (5) and combining them with (6) to (10), we obtain 24 equations with 27 variables (each variable taking values of "0" or "1", representing freedom and constraint, respectively). Clearly, this is an indeterminate equation with multiple solutions. In this paper, we select two sets of solutions as examples, as shown in (11).

$$\mathscr{L}_1 = \begin{Bmatrix} 0 & 1 & 1 & 0 & 1 & 0 \\ 1 & 0 & 0 & 1 & 1 & 0 \\ 1 & 0 & 1 & 0 & 0 & 1 \\ 1 & 1 & 1 & 1 & 1 & 1 \\ 1 & 1 & 1 & 1 & 1 & 1 \\ 1 & 1 & 1 & 1 & 1 & 1 \end{Bmatrix} \tag{11-1}$$

$$\mathscr{L}_2=\begin{Bmatrix}0&1&1&0&1&0\\1&0&0&1&1&0\\1&0&1&0&0&1\\1&0&1&1&1&0\\1&0&1&0&1&1\\1&1&1&0&1&0\end{Bmatrix} \tag{11-2}$$

The compliant modules synthesized from the constraint combinations shown in (11-1) and (11-2) are illustrated in Fig. 4. The two assembled XYZ compliant parallel mechanisms are depicted in Fig. 5(a) and Fig. 5(b). In the following sections, the XYZ compliant parallel mechanism shown in Fig. 5(a) (also proposed by Awtar in 2013 [68]) will be selected for kinetostatic modeling due to its relatively simple structure. Validation will be conducted through finite element simulations, followed by the fabrication and testing of a prototype three-axis force sensor based on this elastic-compliant element.

III. Analytical and Numerical Modeling

This section provides an in-depth exploration of the theoretical analysis and simulation of the XYZ compliant parallel mechanism depicted in Fig. 5(a). An analytical modeling of the XYZ compliant parallel mechanism is conducted using the matrix displacement approach based on node force equilibrium equations [69] to validate the decoupling characteristics of the three-axis force sensor. Subsequently, finite element simulations are performed using the software COMSOL5.3. The finite element simulation results include the analysis of the output displacement-input force relationship and the output force-input force relationship of the three-axis force sensor. In theoretical and numerical modeling, the XYZ compliant parallel mechanism adhere to the fundamental assumptions of material mechanics such as continuum assumption, linear elasticity assumption and small deformation assumption. These results are then compared with the static analytical model to validate the analytical model.

A. Analytical Modeling

The matrix displacement method based on node force equilibrium equations combines the matrix displacement method with the transfer matrix method. It utilizes structural displacement as the fundamental variable, employs matrices for analysis, and utilizes computers to solve various rod system structures' stress and deformation calculations. The essential steps in theoretical modeling for XYZ compliant parallel mechanisms, based on the matrix displacement method, primarily encompass four major stages: (a) Discretization of the structure: The compliant mechanism is discretized into compliant elements and concentrated masses, interconnected by nodes. The compliant elements represent deformable bodies, while the concentrated masses are approximated as rigid bodies. Subsequently, the elements and the nodes connecting them are numbered to facilitate analysis; (b) Elemental analysis: Define the local coordinate system and reference coordinate system of the compliant element. Then calculate the stiffness matrix of the compliant element in the local coordinate system; (c) Coordinate transformation: Convert the stiffness matrix of the compliant element, node displacements, and node forces to the same reference coordinate system, thereby solving for the stiffness matrix of the element in the reference coordinate system; (d) Overall analysis: Sequentially select each node as the focus of study, formulate the force balance equation, and partition the node forces and node displacements for solution, resulting in the determination of the force decoupling measurement model for the XYZ compliant parallel mechanism.

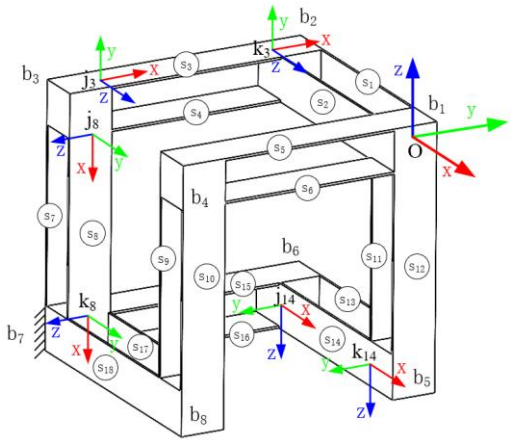

Fig. 6 Discretization of the structure of the compliant elements.

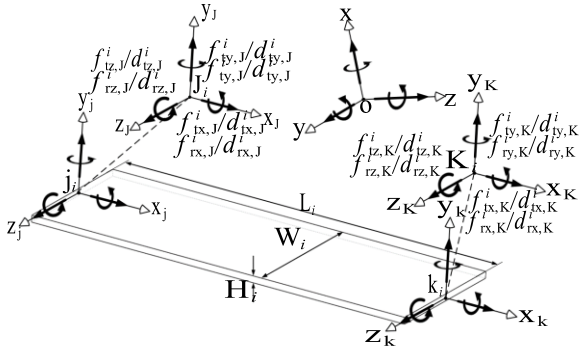

Fig. 7 Local coordinate system and reference coordinate system of S_i, along with actuation forces/torques and displacement responses.

The XYZ compliant parallel mechanism is discretized into several rigid bodies and flexible beam elements, as illustrated in Fig. 6. The rigid bodies are labeled as b_1, b_2…, b_8, while the flexible beam elements are labeled as s_1, s_2…,s_{18}. The two end nodes of s_i are defined as j_i and k_i, and local coordinate systems $\{j_i\}$ and $\{k_i\}$ are established at these nodes. The $\{O\}$ represents the reference coordinate system.

Taking s_i as the research object, as shown in Fig. 7, its nodes j_i and k_i experience force and produce displacement responses, represented by vectors as shown in (12) and (13).

$$\begin{aligned}\boldsymbol{f}_i=[&f^i_{\mathrm{tx,j}},f^i_{\mathrm{ty,j}},f^i_{\mathrm{tz,j}},f^i_{\mathrm{rx,j}},f^i_{\mathrm{ry,j}},f^i_{\mathrm{rz,j}},\\&f^i_{\mathrm{tx,k}},f^i_{\mathrm{ty,k}},f^i_{\mathrm{tz,k}},f^i_{\mathrm{rx,k}},f^i_{\mathrm{ry,k}},f^i_{\mathrm{rz,k}}]^{\mathrm{T}}\end{aligned} \tag{12}$$

$$\begin{aligned}\boldsymbol{d}_i=[&d^i_{\mathrm{tx,j}},d^i_{\mathrm{ty,j}},d^i_{\mathrm{tz,j}},d^i_{\mathrm{rx,j}},d^i_{\mathrm{ry,j}},d^i_{\mathrm{rz,j}},\\&d^i_{\mathrm{tx,k}},d^i_{\mathrm{ty,k}},d^i_{\mathrm{tz,k}},d^i_{\mathrm{rx,k}},d^i_{\mathrm{ry,k}},d^i_{\mathrm{rz,k}}]^{\mathrm{T}}\end{aligned} \tag{13}$$

In the equations, $f^i_{\mathrm{tx,j}}$ represents the force along the X-axis acting on node j_i of s_i, $f^i_{\mathrm{rx,j}}$ represents the moment around the X-axis at node j_i of s_i, $d^i_{\mathrm{tx,j}}$ represents the translational displacement along the X-axis at node j_i of s_i, and $d^i_{\mathrm{rx,j}}$ represents the angular displacement around the x-axis at node j_i of s_i and so on. The nodal force $\boldsymbol{f}_i$ and nodal displacement $\boldsymbol{d}_i$ satisfy (14).

$$\boldsymbol{f}_i=\mathbf{K}_{\text{beam-}i}\cdot\boldsymbol{d}_i \tag{14}$$

where $K_{beam\text{-}i}$ is the stiffness matrix for the unit s_i, and its matrix elements are given by Li in 2022 [67].

The flexible beams are all linked to rigid bodies. Therefore, the nodes j_i and k_i of s_i are relocated to the centroids J_i and K_i of the corresponding rigid bodies, forming extended flexible beams S_i, where the rigid bodies are treated as concentrated masses. Subsequently, the extended stiffness matrix in the local coordinate system is transformed into the reference coordinate system. In Fig. 7, the origins of the centroidal coordinate systems $\{J_i\}$ and $\{K_i\}$ related to s_i have coordinates in the local coordinate system as (x_{ij}, y_{ij}, z_{ij}) and (x_{ik}, y_{ik}, z_{ik}), respectively. The reference coordinate system for the compliant structure is represented as $\{O_{sub}\}$.The relationship between the driving loads $\boldsymbol{F}_i$ and the node displacement responses $\boldsymbol{D}_i$ of S_i in the reference coordinate system $\{O\}$ is given by:

$$\boldsymbol{F}_i = \mathbf{R}_i \cdot \mathbf{T}_i \cdot \mathbf{K}_{beam\text{-}i} \cdot \mathbf{T}_i^{\mathrm{T}} \cdot \mathbf{R}_i^{\mathrm{T}} \cdot \boldsymbol{D}_i \tag{15}$$

where $\mathbf{T}_i$ and $\mathbf{R}_i$ represent the coordinate translation matrix and rotation matrix, respectively, defined as in (16) and (17). In this context, $\boldsymbol{F}_i$ and $\boldsymbol{D}_i$ correspond to the loads and displacements applied at the centroids of the rigid bodies, respectively.

$$\mathbf{T}_i = \begin{bmatrix} \mathbf{T}_{j\text{-}J}^i & \\ & \mathbf{T}_{k\text{-}K}^i \end{bmatrix} \tag{16}$$

$$\mathbf{R}_i = \begin{bmatrix} \mathbf{R}_{j\text{-}O}^i & \mathbf{0} & \mathbf{0} & \mathbf{0} \\ \mathbf{0} & \mathbf{R}_{j\text{-}O}^i & \mathbf{0} & \mathbf{0} \\ \mathbf{0} & \mathbf{0} & \mathbf{R}_{k\text{-}O}^i & \mathbf{0} \\ \mathbf{0} & \mathbf{0} & \mathbf{0} & \mathbf{R}_{k\text{-}O}^i \end{bmatrix} \tag{17}$$

The symbols $\mathbf{T}_{j\text{-}J}^i$ and $\mathbf{T}_{k\text{-}K}^i$ denote the coordinate translation matrices from coordinate systems $\{j_i\}$ to $\{J_i\}$ and from $\{k_i\}$ to $\{K_i\}$, respectively. Their values are given by (18) and (19). The matrices $\mathbf{R}_{j\text{-}O}^i$ and $\mathbf{R}_{k\text{-}O}^i$ represent the rotation matrices from coordinate systems $\{j_i\}$ and $\{k_i\}$ to the reference coordinate system $\{O\}$, and are specifically expressed as in (20) and (21).

$$\mathbf{T}_{j\text{-}J}^i = \begin{bmatrix} 1 & 0 & 0 & 0 & 0 & 0 \\ 0 & 1 & 0 & 0 & 0 & 0 \\ 0 & 0 & 1 & 0 & 0 & 0 \\ 0 & z_{ij} & -y_{ij} & 1 & 0 & 0 \\ -z_{ij} & 0 & x_{ij} & 0 & 1 & 0 \\ y_{ij} & -x_{ij} & 0 & 0 & 0 & 1 \end{bmatrix} \tag{18}$$

$$\mathbf{T}_{k\text{-}K}^i = \begin{bmatrix} 1 & 0 & 0 & 0 & 0 & 0 \\ 0 & 1 & 0 & 0 & 0 & 0 \\ 0 & 0 & 1 & 0 & 0 & 0 \\ 0 & z_{ik} & -y_{ik} & 1 & 0 & 0 \\ -z_{ik} & 0 & x_{ik} & 0 & 1 & 0 \\ y_{ik} & -x_{ik} & 0 & 0 & 0 & 1 \end{bmatrix} \tag{19}$$

$$\mathbf{R}_{j\text{-}O}^i = \begin{bmatrix} \cos\langle x_j^i, x\rangle & \cos\langle y_j^i, x\rangle & \cos\langle z_j^i, x\rangle \\ \cos\langle x_j^i, y\rangle & \cos\langle y_j^i, y\rangle & \cos\langle z_j^i, y\rangle \\ \cos\langle x_j^i, z\rangle & \cos\langle y_j^i, z\rangle & \cos\langle z_j^i, z\rangle \end{bmatrix} \tag{20}$$

$$\mathbf{R}_{k\text{-}O}^i = \begin{bmatrix} \cos\langle x_k^i, x\rangle & \cos\langle y_k^i, x\rangle & \cos\langle z_k^i, x\rangle \\ \cos\langle x_k^i, y\rangle & \cos\langle y_k^i, y\rangle & \cos\langle z_k^i, y\rangle \\ \cos\langle x_k^i, z\rangle & \cos\langle y_k^i, z\rangle & \cos\langle z_k^i, z\rangle \end{bmatrix} \tag{21}$$

In the equation, $\langle x_j^i, x\rangle$ represents the angle between the local coordinate system $\{j_i\}$ x-axis and the reference coordinate system $\{O\}$ x-axis, and similarly for the other terms. Given the above, the stiffness matrix $\mathbf{K}_i$ for s_i in the reference coordinate system is:

$$\mathbf{K}_i = \mathbf{R}_i \cdot \mathbf{T}_i \cdot \mathbf{K}_{beam\text{-}i} \cdot \mathbf{T}_i^{\mathrm{T}} \cdot \mathbf{R}_i^{\mathrm{T}} \tag{22}$$

The coordinates of the centroids of the rigid bodies connected coordinate system are shown in Table III. The angles between the local coordinate system of the flexible beams and the reference coordinate system are presented in Table IV. Let's partition the node forces and node displacements, resulting in:

TABLE III
THE CENTER OF MASS COORDINATES OF THE RIGID BODY CONNECTING THE TWO END NODES OF THE FLEXIBLE BEAM ELEMENT IN THE LOCAL COORDINATE SYSTEM.

	s_1, s_{13}, s_{17}, s_4, s_6, s_{16}, s_7, s_9, s_{11}	s_2, s_{14}, s_{18}, s_3 ,s_5, s_{15}, s_8, s_{10}, s_{12}
x_{ij}	− 0.005	− 0.005
y_{ij}	0.005	− 0.005
z_{ij}	0	0
x_{ik}	0.005	0.005
y_{ik}	0.005	− 0.005
z_{ik}	0	0

TABLE IV
THE ANGLE BETWEEN THE LOCAL COORDINATE SYSTEM AND THE REFERENCE COORDINATE SYSTEM OF THE FLEXIBLE ELEMENT.

	s_1, s_2, s_{13} s_{14}, s_{17}, s_{18}	s_3, s_4, s_5 s_6, s_{15}, s_{16}	s_7, s_8, s_9 s_{10}, s_{11}, s_{12}
$\langle x_{i/k}^i, x\rangle$	0	π/2	π/2
$\langle x_{i/k}^i, y\rangle$	π/2	0	π/2
$\langle x_{i/k}^i, z\rangle$	π/2	π/2	π
$\langle y_{i/k}^i, x\rangle$	π/2	π/2	0
$\langle y_{i/k}^i, y\rangle$	π	π/2	π/2
$\langle y_{i/k}^i, z\rangle$	π/2	0	π/2
$\langle z_{i/k}^i, x\rangle$	π/2	0	π/2
$\langle z_{i/k}^i, y\rangle$	π/2	π/2	π
$\langle z_{i/k}^i, z\rangle$	π	π/2	π/2

$$\boldsymbol{F}_i = \begin{bmatrix} \boldsymbol{F}_{i,\mathrm{J}} \\ \boldsymbol{F}_{i,\mathrm{K}} \end{bmatrix} = \begin{bmatrix} \mathbf{K}_{i,1} & \mathbf{K}_{i,2} \\ \mathbf{K}_{i,3} & \mathbf{K}_{i,4} \end{bmatrix} \cdot \begin{bmatrix} \boldsymbol{D}_{i,\mathrm{J}} \\ \boldsymbol{D}_{i,\mathrm{K}} \end{bmatrix} \tag{23}$$

where $\boldsymbol{F}_{i,\mathrm{j}}$ and $\boldsymbol{F}_{i,\mathrm{k}}$ represent the node forces at the J_i and K_i nodes of S_i, respectively. $\boldsymbol{D}_{i,\mathrm{J}}$ and $\boldsymbol{D}_{i,\mathrm{K}}$ represent the displacements at the J_i and K_i nodes of S_i, respectively. $\mathbf{K}_{i,1}$, $\mathbf{K}_{i,2}$, $\mathbf{K}_{i,3}$, and $\mathbf{K}_{i,4}$ are the block matrices of the stiffness matrix $\mathbf{K}_i$ of S_i in the reference coordinate system. Formulate the node force equilibrium equations:

$$\sum_{i=1}^{N} \boldsymbol{F}_{i,\mathrm{J/K}} = \boldsymbol{\zeta}_n \tag{24}$$

In the equation, N represents the total number of flexible beams connected to b_n, and $\boldsymbol{\zeta}_n$ is the external force acting on the n^{th} node. Sequentially selecting each node of the compliant structure as the subject of study, formulate the system of equations:

$$\begin{bmatrix} \boldsymbol{\zeta}_1 \\ \boldsymbol{\zeta}_2 \\ \boldsymbol{\zeta}_3 \\ \boldsymbol{\zeta}_4 \\ \boldsymbol{\zeta}_5 \\ \boldsymbol{\zeta}_6 \\ \boldsymbol{\zeta}_8 \end{bmatrix} = \begin{bmatrix} \boldsymbol{\Gamma}_1 & \boldsymbol{\Gamma}_9 & & \boldsymbol{\Gamma}_{11} & \boldsymbol{\Gamma}_{15} & & \\ \boldsymbol{\Gamma}_{10} & \boldsymbol{\Gamma}_2 & \boldsymbol{\Gamma}_{13} & & & & \\ & \boldsymbol{\Gamma}_{14} & \boldsymbol{\Gamma}_3 & & & & \\ \boldsymbol{\Gamma}_{12} & & & \boldsymbol{\Gamma}_4 & & & \boldsymbol{\Gamma}_{17} \\ \boldsymbol{\Gamma}_{16} & & & & \boldsymbol{\Gamma}_5 & \boldsymbol{\Gamma}_{19} & \\ & & & & \boldsymbol{\Gamma}_{20} & \boldsymbol{\Gamma}_6 & \\ & & & \boldsymbol{\Gamma}_{18} & & & \boldsymbol{\Gamma}_8 \end{bmatrix} \cdot \begin{bmatrix} \boldsymbol{\xi}_1 \\ \boldsymbol{\xi}_2 \\ \boldsymbol{\xi}_3 \\ \boldsymbol{\xi}_4 \\ \boldsymbol{\xi}_5 \\ \boldsymbol{\xi}_6 \\ \boldsymbol{\xi}_8 \end{bmatrix} \tag{25}$$

where $\boldsymbol{\zeta}_n$ is the input force at node n, and $\boldsymbol{\xi}_n$ is the nodal displacement at node n. The matrix elements $\boldsymbol{\Gamma}_i$ take values as defined in (26).

$$\begin{cases} \boldsymbol{\Gamma}_1 = \mathbf{K}_{1,4} + \mathbf{K}_{2,4} + \mathbf{K}_{5,4} + \mathbf{K}_{6,4} + \mathbf{K}_{11,1} + \mathbf{K}_{12,1}; \\ \boldsymbol{\Gamma}_2 = \mathbf{K}_{1,1} + \mathbf{K}_{2,1} + \mathbf{K}_{3,4} + \mathbf{K}_{4,4};\ \boldsymbol{\Gamma}_{12} = \mathbf{K}_{5,2} + \mathbf{K}_{6,2}; \\ \boldsymbol{\Gamma}_3 = \mathbf{K}_{3,1} + \mathbf{K}_{4,1} + \mathbf{K}_{7,1} + \mathbf{K}_{8,1};\ \boldsymbol{\Gamma}_{13} = \mathbf{K}_{3,3} + \mathbf{K}_{4,3}; \\ \boldsymbol{\Gamma}_4 = \mathbf{K}_{5,1} + \mathbf{K}_{6,1} + \mathbf{K}_{9,1} + \mathbf{K}_{10,1};\ \boldsymbol{\Gamma}_{14} = \mathbf{K}_{3,2} + \mathbf{K}_{4,2}; \\ \boldsymbol{\Gamma}_5 = \mathbf{K}_{11,4} + \mathbf{K}_{12,4} + \mathbf{K}_{13,4} + \mathbf{K}_{14,4};\ \boldsymbol{\Gamma}_{15} = \mathbf{K}_{11,2} + \mathbf{K}_{12,2}; \\ \boldsymbol{\Gamma}_6 = \mathbf{K}_{13,1} + \mathbf{K}_{14,1} + \mathbf{K}_{15,4} + \mathbf{K}_{16,4};\ \boldsymbol{\Gamma}_{16} = \mathbf{K}_{11,3} + \mathbf{K}_{12,3}; \\ \boldsymbol{\Gamma}_8 = \mathbf{K}_{9,4} + \mathbf{K}_{10,4} + \mathbf{K}_{17,4} + \mathbf{K}_{18,4};\ \boldsymbol{\Gamma}_{17} = \mathbf{K}_{9,2} + \mathbf{K}_{10,2}; \\ \boldsymbol{\Gamma}_9 = \mathbf{K}_{1,3} + \mathbf{K}_{2,3};\ \boldsymbol{\Gamma}_{18} = \mathbf{K}_{9,3} + \mathbf{K}_{10,3}; \\ \boldsymbol{\Gamma}_{10} = \mathbf{K}_{1,2} + \mathbf{K}_{2,2};\ \boldsymbol{\Gamma}_{19} = \mathbf{K}_{13,3} + \mathbf{K}_{14,3}; \\ \boldsymbol{\Gamma}_{11} = \mathbf{K}_{5,3} + \mathbf{K}_{6,3};\ \boldsymbol{\Gamma}_{20} = \mathbf{K}_{13,2} + \mathbf{K}_{14,2}; \end{cases} \tag{26}$$

In the elastic-compliant element, the rigid body b_1 is used to measure the external force $\boldsymbol{F}_{ext}$ and satisfies (27).

$$\boldsymbol{\zeta}_1 = \mathbf{T}_{ext} \cdot \boldsymbol{F}_{ext} \tag{27}$$

where the $\mathbf{T}_{ext}$ in the equation is the transformation matrix that converts the external force to the centroid of the rigid body, and its values are as follows:

$$\mathbf{T}_{ext} = \begin{bmatrix} 1 & 0 & 0 & 0 & 0 & 0 \\ 0 & 1 & 0 & 0 & 0 & 0 \\ 0 & 0 & 1 & 0 & 0 & 0 \\ 0 & -0.005 & 0.005 & 1 & 0 & 0 \\ 0.005 & 0 & -0.005 & 0 & 1 & 0 \\ -0.005 & 0.005 & 0 & 0 & 0 & 1 \end{bmatrix} \tag{28}$$

Rigid bodies b_3, b_8, and b_6 are rigidly attached to pressure sensors, measuring forces in the x, y, and z directions, respectively. Therefore:

$$\boldsymbol{\zeta}_2 = \boldsymbol{\zeta}_4 = \boldsymbol{\zeta}_5 = \mathbf{0} \tag{29}$$

$$\boldsymbol{\xi}_3 = \boldsymbol{\xi}_6 = \boldsymbol{\xi}_8 = \mathbf{0} \tag{30}$$

$$\boldsymbol{F}_{mea} = [F_x, F_y, F_z]^{\mathrm{T}} = [-\boldsymbol{\zeta}_3(1), -\boldsymbol{\zeta}_8(2), -\boldsymbol{\zeta}_6(3)]^{\mathrm{T}} \tag{31}$$

where $\boldsymbol{F}_{mea}$ represents the measured force, and F_x, F_y, F_z respectively denote the unidirectionally decoupled forces sensed by the pressure sensors at b_3, b_8, and b_6.

Substituting (27) to (31) into (25) and solving the resulting system of equations, we obtain the force-decoupling measurement model:

$$\boldsymbol{F}_{mea} = \begin{bmatrix} \mathbf{K}_x^{1,:} \\ \hline \mathbf{K}_y^{2,:} \\ \hline \mathbf{K}_z^{3,:} \end{bmatrix} \cdot \boldsymbol{F}_{ext} \tag{29}$$

B. Finite Element Analysis

To validate the analytical model for the XYZ compliant parallel mechanism, finite element simulations are conducted in this study. The geometric dimensions are illustrated in Fig. 11(a) and summarized in Table V. The material chosen for the simulations is aluminum alloy 7075, with a Young's modulus E of 71.7GPa, and a Poisson's ratio μ of 0.3. To mitigate the influence of the base on the deformation of the elastic module and the movement of the rigid module, the loading range for the finite element simulation model is set from 0 to 1000 g. The commercial software COMSOL5.3 was employed with a 10-node tetrahedral mesh, using default refinement parameters (maximum element size of 3.6 mm, minimum of 0.262 mm, maximum element growth rate of 1.4, curvature factor of 0.4, and resolution in narrow regions set to 0.7). The XYZ compliant parallel mechanism comprises parallelogram mechanisms, which exhibit high linearity, allowing the overall mechanism to be considered linear. In the FEM analysis, a linear elastic material under static load was selected for simulation. The results obtained with a linear solver closely matched those from a nonlinear solver. To expedite simulation time, the PARDISO solver was employed. The specific finite element simulation process is illustrated in Fig. 8.

The input-output relationship curve of the three-axis force sensor is shown in Fig. 9. From Fig. 9, it can be observed that: (1) the results of finite element analysis and the analytical model of input-output curves are matched well, with an average difference of around 0.1%; (2) as the input force along the X-axis gradually increases, the output force of the X-ORM shows growth with high linearity; (3) when only an external force is applied in the X direction, the output forces measured by the Y-ORM and Z-ORM are relatively low, and the maximum cross-axis coupling error is 1.8%, indicating minimal coupling influence. These results demonstrate that the proposed XYZ compliant parallel mechanism can effectively decompose spatial three-axis forces into orthogonal single forces along three directions, achieving excellent decoupling performance.

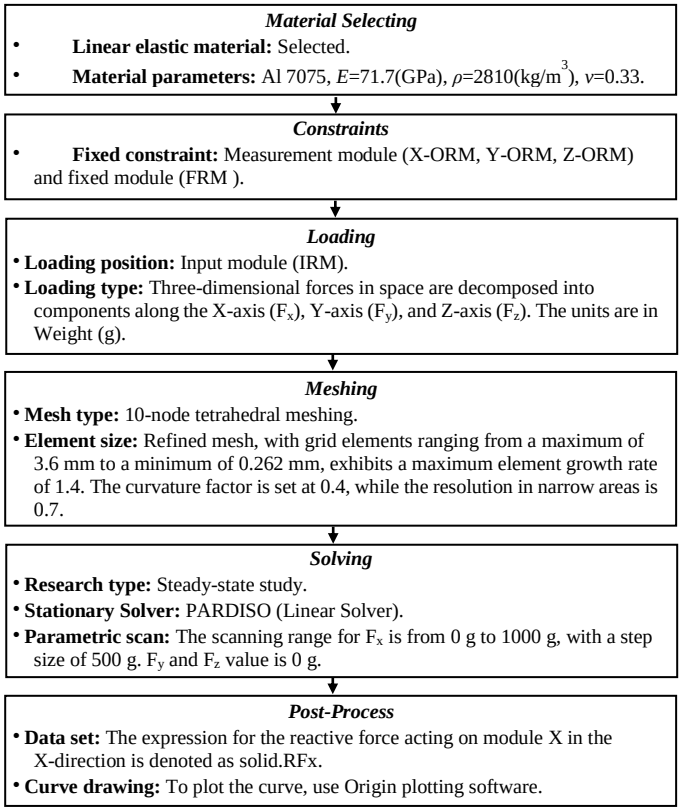

Fig. 8 A flowchart for finite element numerical analysis of the input-output force relationship in elastic compliant elements.

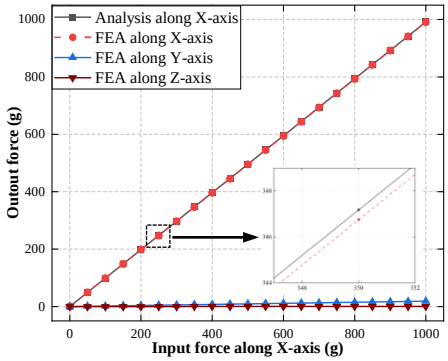

Fig. 9 Curves depicting the variations of the output forces from X-ORM, Y-ORM, and Z-ORM in response to the transformation of the input force along the X-axis of IRM.

IV. Experimental Testing

In this section, based on the designed XYZ compliant parallel mechanism discussed earlier, the system design of the three-axis force sensor is completed. A prototype experimental setup of the three-axis force sensor is established to further validate the correctness of the theoretical models (finite element model and analysis model) and the decoupling characteristics of the three-axis force sensor.

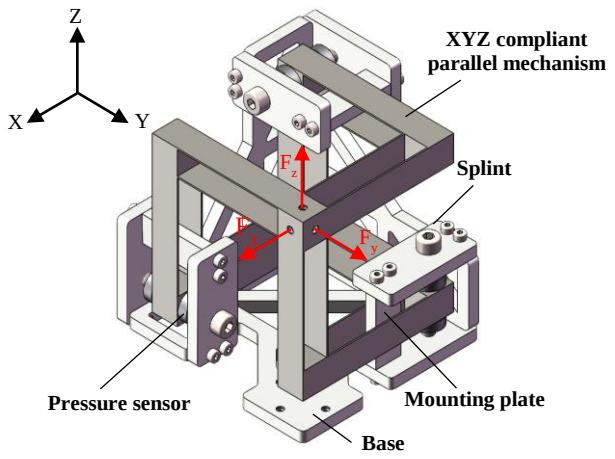

Fig. 10 Structure of the three-axis force sensor.

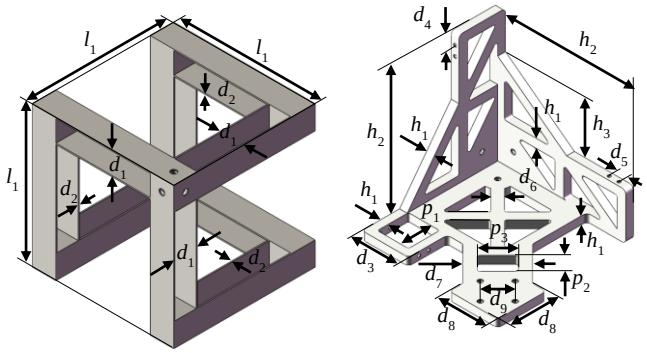

(a) (b)

Fig. 11 Dimensions of the parts of the three-axis force sensor: (a) XYZ compliant parallel mechanism, (b) Base.

TABLE Ⅴ
GEOMETRIC DIMENSIONS OF THE DESIGN SHOWN IN FIG. 11.

Parameter	Value	Parameter	Value	Parameter	Value
l_1	60 mm	d_6	5 mm	h_3	46 mm
d_1	10 mm	d_7	25.5 mm	p_1	16 mm
d_2	0.5 mm	d_8	25 mm	p_2	10 mm
d_3	24 mm	d_9	12.7 mm	p_3	15 mm
d_4	5.5 mm	h_1	4 mm		
d_5	5 mm	h_2	66 mm		

As illustrated in Fig. 10, the three-axis force sensor is primarily comprised of three main components: the XYZ compliant parallel mechanism, unidirectional force measurement units, and the base. The structure of the XYZ compliant parallel mechanism includes rigid modules (FRM, ORM, and IRM) and the compliant modules (GCM and DCM). The FRM is securely attached to the base, providing support for the entire XYZ compliant parallel mechanism. The IRM receives spatial three-axis forces, and the X-ORM, Y-ORM, and Z-ORM, in contact with the pressure sensors of the unidirectional force measurement units, measure the various components of spatial three-axis forces. The unidirectional force measurement unit is composed of pressure sensors, clamping plates, and support plates. The clamping plates on both sides are affixed to the base and interconnected through the support plate. Pressure sensors apply pre-tightening force via bolts on both sides of the clamping plates, securing them at the flanks of ORMs of the XYZ compliant parallel mechanism. The base is utilized to support and fix both the XYZ compliant parallel mechanism and unidirectional force measurement units. On one hand, it provides constraints from the ground to the XYZ compliant parallel mechanism, and on the other hand, it serves to fix the pressure sensor for easy collection of the decomposed uniaxial forces. This arrangement facilitates the measurement of spatial three- axis force components transmitted to the measurement module.

Taking the X-direction measurement as an example, when the IRM experiences spatial three-axis forces, the XYZ compliant parallel mechanism transmits the X-direction force component to the X-ORM, resulting in an increase (or decrease) in the pre-tightening force at both ends of the ORM. The difference in pre-tightening force transformation is then calculated to determine the component of the spatial vector force in the X-direction.

The key part of the design, shown in Fig. 11, has been manufactured mainly using wire electrical discharge machining. The prototype experimental setup for the three-axis force sensor, constructed based on the topological diagram in Fig. 1, is illustrated in Fig. 12. This apparatus utilizes a combination of weights with a resolution of 10g and a maximum range of 1.8kg to provide input forces. The pressure sensor employed for measuring output forces (HZC-MH1, from Chengying Sensor) features a sensitivity of 1.5±0.2 mv/V, a maximum range of 5 kg, an overall accuracy of 0.5% F·S, a nonlinearity precision of ±0.5% F·S, repeatability error of ±0.5% F·S, and hysteresis error of ±0.5% F·S. The sensor's overall dimensions are a diameter of 10 mm and a thickness of 3 mm. The output signals from the pressure sensor are transmitted through a signal amplifier (LZ-740, from Lizhun Sensor) to a semi-physical simulation machine (WIPC-710, from Huachuang Instrument Technology), ultimately displayed and stored on a computer.

By analyzing the relationship between input forces and output forces under external forces in different directions, the decoupling characteristics of the three-axis force sensor are examined. Fig. 13(a) illustrates the measurement results of the X-ORM obtained from finite element simulations, analytical modeling, and experimental testing under external forces along the X-axis. Similarly, Figures 13(b) and (c) show the measurement results under external forces along the Y-axis and Z-axis, respectively. It can be observed that, in the dimension of the applied input force, the experimental input-output force curves of the three-axis force sensor exhibit a high parallelism with the analytical model result curves, both increasing approximately at a 45-degree angle with the growing input force. The outputs in other directions fluctuate below 20g, indicating a relatively small cross-axis coupling effect from the input force dimension. Figures 13(d), (e), and (f) show the coupling errors in each direction of the three-axis force sensor, with a maximum coupling error of 3.3%. The average cross-axis coupling errors are 1.41% between X and Y-axes, 1.75% between Y and Z-axes, and 1.50% between X and Z-axes. It is also noteworthy that the experimental testing results are higher than those of the finite element model and analysis model, possibly due to manufacturing errors, assembly errors, and measurement errors. The coupling errors of the state-of-the-art multi-axis force sensors introduced in [9], [39] and [50] are 2%, 1.64% and 2.76% respectively. The average pre-calibrated coupling error of the three-axis force sensor proposed in this paper is around 1.5%.

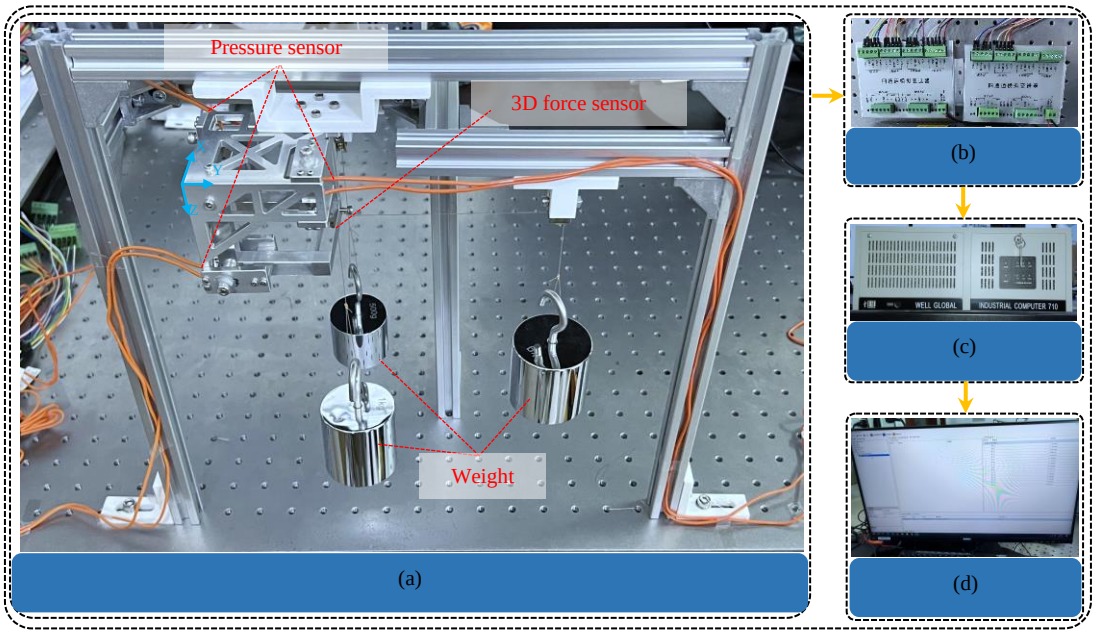

Fig. 12 Prototype and the experimental testing setup: (a) Prototype (b) Signal amplifier (c) Semi-physical simulator (d) Computer.

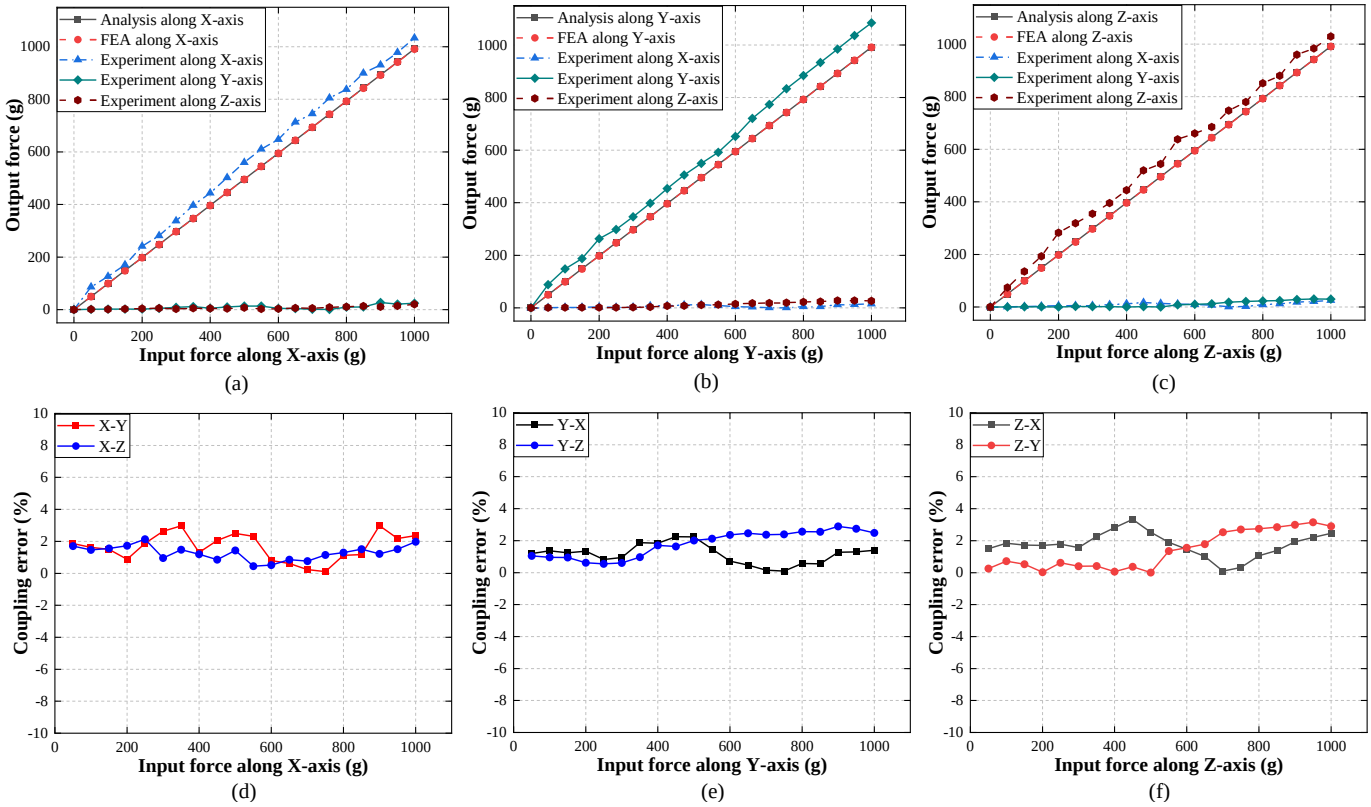

Fig. 13 Input force and Output force relationships and coupling errors among X, Y and Z-axes: (a) With loading along X-axis; (b) With loading along Y-axis; (c) With loading along Z-axis; (d) Coupling errors with loading along X-axis; (d) Coupling errors with loading along Y-axis; (e) Coupling errors with loading along Z-axis.

V. Conclusion

This paper presents a novel design concept for multi-axis force sensors, employing decoupled compliant parallel mechanisms with an innovative measuring principle. This pioneering concept effectively addresses the challenges of balancing sensitivity and measuring range, while also minimizing cross-axis coupling errors. The paper commences by introducing the novel design concept, followed by a detailed case study featuring a self-decoupling three-axis force sensor in the X, Y, and Z directions based on this design concept.

Initially, a comprehensive approach is adopted to synthesize XYZ compliant parallel mechanisms with reduced cross-axis coupling errors, intended as the elastic-sensitive components for three-axis force sensors. Utilizing the constraint flow

approach, multiple sets of permissible constraint combinations are generated to meet the decoupling requirements, with detailed explanations of two such combinations. Subsequently, two XYZ compliant parallel mechanisms are synthesized based on one of the constraint combinations, with one of these mechanisms selected for further analysis. The chosen XYZ compliant parallel mechanism undergoes analytical modeling using the matrix displacement method, followed by finite element simulations. The results revealed a close alignment between the analytical and numerical models, with differences around 0.1% and approximately 0.8% cross-axis coupling errors.

Following this, a three-axis force sensor prototype based on the XYZ compliant parallel mechanism is fabricated and subjected to experimental testing. The results demonstrated that the proposed three-axis force sensor in the study exhibited a mere 1.5% pre-calibration coupling error, indicative of exceptional decoupling characteristics. In comparison with strain-gauge-based multi-axis force sensors, the proposed three-axis force sensor showcased an impressive 8% reduction in coupling error. Notably, the measuring sensitivity of the proposed three-axis force sensor is not solely reliant on the deformation sensitivity of the XYZ compliant parallel mechanism. This suggests that the XYZ compliant parallel mechanism does not necessitate low stiffness in the deformation directions to achieve high measuring sensitivity, thus suggesting the potential for a substantial measuring range with minimal cross-axis coupling errors.

Looking ahead, future work will involve the design of a more compact prototype utilizing alternative sensing elements, such as piezoelectric ceramics. Furthermore, the signal processing systems and nonlinear dynamic characteristics will be explored.

REFERENCES

[1] L. Xiong, G. Jiang, Y. Guo, and H. Liu, "A three-dimensional fiber Bragg grating force sensor for robot," *IEEE Sensors J.*, vol. 18, no. 9, pp. 3632-3639, May. 2018.

[2] U. Kim, D. Lee, Y. B. Kim, D. Seok, and H. R. Choi, "A novel six-axis force/torque sensor for robotic applications," *IEEE/ASME Trans. Mechatronics.*, vol. 22, no. 3, pp. 1381-1391, Jun. 2017.

[3] P. Billeschou, C. Albertsen, J. C. Larsen, and P. Manoonpong, "A low-cost, compact, sealed, three-axis force/torque sensor for walking robots," *IEEE* Sensors *J.*, vol. 21, no. 7, pp. 8916-8926, Apr. 2021.

[4] A. Tar and G. Cserey, "Development of a low cost 3D optical compliant tactile force sensor," in *Proc. 2011 IEEE/ASME Int. Conf. Adv. Intell. Mechatronics (AIM)*, Jul. 2011, pp. 236-240.

[5] P. Yu, W. Liu, C. Gu, X. Cheng, and X. Fu, "Flexible piezoelectric tactile sensor array for dynamic three-axis force measurement," *Sensors*, vol. 16, no. 6, p. 819, Jun. 2016.

[6] Y. Yan, Z. Hu, Z. Yang, W. Yuan, C. Song, J. Pan, and Y. Shen, "Soft magnetic skin for super-resolution tactile sensing with force self-decoupling," *Sci. Robot.*, vol. 6, no. 51, p. eabc8801, Feb. 2021.

[7] P. Puangmali, K. Althoefer, L. D. Seneviratne, D. Murphy, and P. Dasgupta, "State-of-the-art in force and tactile sensing for minimally invasive surgery," *IEEE Sensors J.*, vol. 8, no. 4, pp. 371-381, Apr. 2008.

[8] R. Haslinger, P. Leyendecker, and U. Seibold, "A fiberoptic force-torque-sensor for minimally invasive robotic surgery," in *Proc. 2013 IEEE Int. Conf. Robot. Automat. (ICRA)*, May. 2013, pp. 4390-4395.

[9] F. Herbst, R. Chadda, C. Hartmann, J. Peters, D. Riehl, T. Gwosch, K. Hofmann, S. Matthiesen, and M. Kupnik, "Multi-axis force sensor for sensor-integrating bolts," in *Proc. 2022 IEEE Sensors*, Dec. 2022, pp. 1-4.

[10] G. Lin, H. Pang, W. Zhang, D. Wang, and L. Feng, "A self-decoupled three-axis force sensor for measuring the wheel force," *Proc. Institution Mech. Engineers, Part D: J. Automobile Eng.*, vol. 228, no. 3, pp. 319-334, Feb. 2014.

[11] L. Feng, G. Lin, W. Zhang, H. Pang, and T. Wang, "Design and optimization of a self-decoupled six-axis wheel force transducer for a heavy truck," *Proc. Institution Mech. Engineers, Part D: J. Automobile Eng.*, vol. 229, no. 12, pp. 1585-1610, Oct. 2015.

[12] Y. Sun, Y. Liu, T. Zou, M. Jin, and H. Liu, "Design and optimization of a novel six-axis force/torque sensor for space robot," *Measurement*, vol. 65, pp. 135-148, Jan. 2015.

[13] Y. Guo, J. Kong, H. Liu, H. Xiong, G. Li, and L. Qin, "A three-axis force fingertip sensor based on fiber Bragg grating," *Sens. Actuators A: Phys.*, vol. 249, pp. 141-148, Aug. 2016.

[14] J. O. Templeman, B. B. Sheil, and T. Sun, "Multi-axis force sensors: A state-of-the-art review," *Sens. Actuators A: Phys.*, vol. 304, p. 111772, Apr. 2020.

[15] B. Wu and P. Cai, "Decoupling analysis of a sliding structure six-axis force/torque sensor," *Meas. Sci. Rev.*, vol. 13, no. 4, pp. 187-193, Aug. 2013.

[16] D. Nguyen and C. Kuo, "Design and optimization of a joint torque sensor for lightweight robots," *IEEE Sensors J.*, vol. 21, no. 8, pp. 9788-9797, Apr. 2021.

[17] S. Hu, H. Wang, Y. Wang, and Z. Liu, "Design of a novel six-axis wrist force sensor," *Sensors*, vol. 18, no. 9, p. 3120, Sep. 2018.

[18] R. Shu, Z. Chu, and H. Shu, "A lever-type method of strain exposure for disk F-Shaped torque sensor design," *Sensors*, vol. 20, no. 2, p. 541, Jan. 2020.

[19] Y. Wang, J. Zheng, G. Ren, P. Zhang, and C. Xu, "A flexible piezoelectric force sensor based on PVDF fabrics," *Smart Mater. Struct.*, vol. 4, no. 20, p. 045009, Mar. 2011.

[20] E. J. Curry, K. Ke, M. T. Chorsi, K. S. Wrobel, A. N. Miller, A. Patel, I. Kim, J. Feng, L. Yue, Q. Wu, C. Kuo, K. W. H. Lo, C. T. Laurencin, H. Ilies, P. K. Purohit, and T. D. Nguyen, "Biodegradable piezoelectric force sensor," *Proc. Nat. Acad. Sci.*, vol. 115, no. 5, pp. 909-914, Jan. 2018.

[21] M. Fontana, S. Marcheschi, F. Salsedo, and M. Bergamasco, "A three-axis force sensor for dual finger haptic interfaces," *Sensors*, vol. 12, no. 10, pp. 13598-13616, Oct. 2012.

[22] P. Roriz, L. Carvalho, O. Frazão, J. L. Santos, and J. A. Simões, "From conventional sensors to fibre optic sensors for strain and force measurements in biomechanics applications: A review," *J. Biomechanics*, vol. 47, no. 6, pp. 1251-1261, Apr. 2014.

[23] R. Xu, A. Yurkewich, and R. V. Patel, "Curvature, torsion, and force sensing in continuum robots using helically wrapped FBG sensors," *IEEE Robot. Autom. Lett.*, vol. 1, no. 2, pp. 1052-1059, Jul. 2016.

[24] X. He, J. Handa, P. Gehlbach, R. Taylor, and I. Iordachita, "A submillimetric 3-DOF force sensing instrument with integrated fiber Bragg grating for retinal microsurgery," *IEEE Trans. Biomed. Eng.*, vol. 61, no. 2, pp. 522-34, Feb. 2014.

[25] X. Zhang, Z. Zheng, L. Wang, H. Cui, X. Xie, H. Wu, X. Liu, B. Gao, H. Wang, and P. Xiang, "A quasi-distributed optic fiber sensing approach for interlayer performance analysis of ballastless track-type II plate," *Opt. Laser Technol.*, vol. 170, p. 110237, Mar. 2024.

[26] J. Palmowski, K. Barczak, N. Kubicka, F. Gołek, L. Benson, E. Maciak, T. Pustelny, S. Phang, T. Benson, and E. Bereś-Pawlik, "Optical strain sensor with dual fibre Bragg grating topology," *Opt. Quantum Electron.*, vol. 55, no. 5, Mar. 2023.

[27] Y. Sun, Y. Liu, M. Jin, and H. Liu, "Design and optimization of a novel six-axis force/torque sensor with good isotropy and high sensitivity," in *Proc. 2013 IEEE Int. Conf. Robot. Biomimetics (ROBIO)*, Dec. 2013, pp. 631-638.

[28] A. Song and L. Fu, "Multi-dimensional force sensor for haptic interaction: a review," *Virtual Reality Intell. Hardware*, vol. 1, no. 2, pp. 121-135, Apr. 2019.

[29] J. Lei, L. Qiu, M. Liu, Q. Song, and Y. Ge, "Application of neural network to nonlinear static decoupling of robot wrist force sensor," in *Proc. 2006 6th World Congr. on Intell. Control Automa.*, Jun. 2016, pp. 5282-5285.

[30] L. Fu and A. Song, "An optimized BP neural network based on genetic algorithm for static decoupling of a six-axis force/torque sensor," *IOP Conf. Ser.: Mater. Sci. Eng.*, vol. 311, no. 1, p. 12002, Feb. 2018.

[31] S. Chen, H. Wang, L. Du, and J. Li, "Research on a new type of overvoltages monitoring sensor and decoupling technology," *IEEE Trans. Appl. Supercond.*, vol. 24, no. 5, pp. 1-4, Oct. 2014.

[32] Y. Song, F. Wang, and Z. Zhang, "Decoupling research of a novel three-dimensional force flexible tactile sensor based on an improved BP algorithm," *Micromachines*, vol. 9, no. 5, p. 236, May. 2018.

[33] Q. Liu, Y. Dai, M. Li, B. Yao, Y. Xin, and J. Zhang, "Real-time processing of force sensor signals based on LSTM-RNN," in *Proc. 2022 IEEE Int. Conf. Robot. Biomimetics (ROBIO)*, Dec. 2022, pp. 167-171.

[34] Y. Wang, L. Wu, J. Ke, and T. Lu, "Planar six-axis force and torque sensors," *IEEE Sensors J.*, vol. 21, no. 23, pp. 26631-26641, Dec. 2021.
[35] Q. Pan, X. Kang, H. Wang, J. Luo, F. Wang, J. Tang, and Z. Han, "Design and analysis of a miniature self-decoupling six-dimensional force/moment sensor," *Proc. Institution Mech. Engineers, Part C: J. Mech. Eng. Sci.*, vol. 238, no. 1, pp. 203-217, Jan. 2024.
[36] M. Kang, S. Lee, and J. Kim, "Shape optimization of a mechanically decoupled six-axis force/torque sensor," *Sens. Actuators A: Phys.*, vol. 209, pp. 41-51, Mar. 2014.
[37] G. Mastinu, M. Gobbi, and G. Previati, "A new six-axis load cell. Part I: Design," *Exp. Mech.*, vol. 51, no. 3, pp. 373-388, Mar. 2011.
[38] Z. Niu, T. Zhao, Y. Zhao, Q. Hu, and S. Ding, "Design and analysis of the measurement characteristics of a bidirectional-decoupling over-constrained six-dimensional parallel-mechanism force sensor," Sensors, vol. 17, no. 9, p. 1985, Aug. 2017.
[39] J. Yao, L. Zu, H. Ruan, D. Cai, Y. Xu, and Y. Zhao, "A heavy load miniature six-component force sensing mechanism with hybrid branches," *Measurement*, vol. 157, p. 107623, Jun. 2020.
[40] G. Kim, "Design of a six-axis wrist force/moment sensor using FEM and its fabrication for an intelligent robot," *Sens. Actuators A: Phys.*, vol. 133, no. 1, pp. 27-34, Jan. 2007.
[41] J. E. Sanders, R. A. Miller, D. N. Berglund, and S. G. Zachariah, "A modular six-directional force sensor for prosthetic assessment: a technical note," *J. Rehabil. Res. Dev.*, vol. 34, no. 2, pp. 195-202, Apr. 1997.
[42] B. H. Lee and J. W. Joo, "Design of six-component F/T sensor with flexible fixed ends," *Trans. Korean Soc. Mech. Engineers A*, vol. 34, no. 6, pp. 771-780, Jun. 2010.
[43] G. Hao, M. Murphy, and X. Luo, "Development of a compliant-mechanism-based compact three-axis force sensor for high-precision manufacturing," in *Proc. ASME 2015 Int. Des. Eng. Tech. Conf. Comput. Inf. Eng. Conf.*, Aug. 2015, pp. V009T07A082.
[44] L. L. Howell, S. S. Rao, and A. Midha, "Reliability-based optimal design of a bistable compliant mechanism," *J. Mech. Des.*, vol. 116, no. 4, pp. 1115-1121, Dec. 1994.
[45] J. Yu, G. Hao, G. Chen, and S. Bi, "State-of-art of compliant mechanisms and their applications," *J. Mech. Eng.*, vol. 13, no. 51, pp. 53-68, Jul. 2015.
[46] Y. Yang, Y. Wei, J. Lou, F. Xie, and L. Fu, "Development and precision position/force control of a new flexure-based microgripper," *J. Micromech. Microeng.*, vol. 26, no. 1, pp. 15005-19, Dec. 2015.
[47] J. Jiang, W. Chen, J. Liu, W. Chen, and J. Zhang, "Optimum design of a dual-range force sensor for achieving high sensitivity, broad bandwidth, and large measurement range," *IEEE Sensors J.*, vol. 15, no. 2, pp. 1114-1123, Feb. 2015.
[48] A. G. Dunning, N. Tolou, and J. L. Herder, "Review article: Inventory of platforms towards the design of a statically balanced six degrees of freedom compliant precision stage," *Mech. Sci.*, vol. 2, no. 2, pp. 157-168, Aug. 2011.
[49] Y. Wang, C. Hsu, and C. Sue, "Design and calibration of a dual-frame force and torque sensor," *IEEE Sensors J.*, vol. 20, no. 20, pp. 12134-12145, Oct. 2020.
[50] S. Matich, M. Hessinger, M. Kupnik, R. Werthschützky, and C. Hatzfeld, "Miniaturized multiaxial force/torque sensor with a rollable hexapod structure: miniaturisierter kraft-momenten-sensor auf basis einer gerollten hexapod-struktur," *TM-Technisches Messen*, vol. 84, no. s1, pp. 138-142, Sep. 2017.
[51] G. Chen, Y. Gou, and A. Zhang, "Synthesis of compliant multistable mechanisms through use of a single bistable mechanism," *J. Mech. Des.*, vol. 133, no. 8, p. 081007, Aug. 2011.
[52] B. Zhu, Q. Chen, H. Li, H. Zhang, and X. Zhang, "Design of planar large-deflection compliant mechanisms with decoupled multi-input-output using topology optimization," *J. Mechanisms Robot.*, vol. 11, no. 3, p. 031015, Jun. 2019.
[53] Z. Zhang, X. Yang, and P. Yan, "Large dynamic range tracking of an XY compliant nanomanipulator with cross-axis coupling reduction," *Mech. Syst. Signal Process.*, vol. 117, pp. 757-770, Feb. 2019.
[54] H. Li, G. Hao, and R. C. Kavanagh, "Position-space-based compliant mechanism reconfiguration approach and its application in the reduction of parasitic motion," *J. Mech. Des.*, vol. 138, no. 9, p. 092301, Sep. 2016.
[55] N. C. Archer and J. B. Hopkins, "Large-range rotation-to-translation compliant transmission mechanism," *J. Mech. Des.*, vol. 145, no. 12, p. 125001, Dec. 2023.
[56] J. M. Derderian, L. L. Howell, M. D. Murphy, S. M. Lyon, and S. D. Pack, "Compliant parallel-guiding mechanisms," in *Proc. ASME 1996 Des. Eng. Tech. Conf. Comput. Eng. Conf.*, Aug. 1996, p. V0AT02A017.
[57] C. A. Mattson, L. L. Howell, and S. P. Magleby, "Development of commercially viable compliant mechanisms using the pseudo-rigid-body model: case studies of parallel mechanisms," *J. Intell. Mater. Syst. Struct.*, vol. 15, no. 3, pp. 195-202, Mar. 2004.
[58] J. B. Hopkins, K. J. Lange, and C. M. Spadaccini, "Synthesizing the compliant microstructure of thermally actuated materials using freedom, actuation, and constraint topologies," in *Proc. ASME 2012 Int. Des. Eng. Tech. Conf. Comput. Inf. Eng. Conf.*, Aug. 2012, pp. 249-258.
[59] C. M. DiBiasio and J. B. Hopkins, "Sensitivity of freedom spaces during flexure stage design via FACT," *Precis. Eng.*, vol. 36, no. 3, pp. 494-499, Jul. 2012.
[60] S. R. Deepak, M. Dinesh, D. K. Sahu, and G. K. Ananthasuresh, "A comparative study of the formulations and benchmark problems for the topology optimization of compliant mechanisms," *J. Mechanisms Robot.*, vol. 1, no. 1, p. 011003, Feb. 2019.
[61] F. Dirksen, T. Berg, R. Lammering, and T. I. Zohdi, "Topology synthesis of large-displacement compliant mechanisms with specific output motion paths," *Proc. Appl. Math. Mech.*, vol. 12, no. 1, pp. 801-804, Dec. 2012.
[62] C. B. W. Pedersen, T. Buhl, and O. Sigmund, "Topology synthesis of large-displacement compliant mechanisms," *Int. J. Numer. Methods Eng.*, vol. 50, no. 12, pp. 2683-2705, Feb. 2001.
[63] K. Liang, D. Zhu, and J. Liu, "Topology optimization of a spatial compliant parallel mechanism based on constant motion transmission characteristic matrix," *Mechanism Mach. Theory*, vol. 180, p. 105125, Feb. 2023.
[64] S. S, C. LF, and H. A, "Topology-optimization based design of multi-degree-of-freedom compliant mechanisms (mechanisms with multiple pseudo-mobility)," *J. Intell. Mater. Syst. Struct.*, vol. 34, no. 5, pp. 609-628, Aug. 2023.
[65] Y. Sun, Y. Liu, L. Xu, and T. C. Lueth, "Design of a disposable compliant medical forceps using topology optimization techniques," in *Proc. 2019 IEEE Int. Conf. Robot. Biomimetics (ROBIO)*, Dec. 2019, pp. 924-929.
[66] H. Li and G. Hao, "A constraint and position identification (CPI) approach for the synthesis of decoupled spatial translational compliant parallel manipulators," *Mechanism Mach. Theory*, vol. 90, pp. 59-83, Aug. 2015.
[67] H. Li, Y. Liu, Z. Wang, C. Leng, Z. Zhang, and G. Hao, "A constraint-flow based method of synthesizing XYθ compliant parallel mechanisms with decoupled motion and actuation characteristics," *Mechanism Mach. Theory*, vol. 178, p. 105085, Dec. 2022.
[68] S. Awtar, J. Ustick, and S. Sen, "An XYZ parallel-kinematic flexure mechanism with geometrically decoupled degrees of freedom," *J. Mechanisms Robot.*, vol. 5, no. 1, p. 015001, Feb. 2013.
[69] M. Ling, J. Cao, L. L. Howell, and M. Zeng, "Kinetostatic modeling of complex compliant mechanisms with serial-parallel substructures: A semi-analytical matrix displacement method," *Mechanism Mach. Theory*, vol. 125, pp. 169-184, Mar. 2018.

Haiyang Li is an Associate Professor in School of Mechanical Engineering at Dalian University of Technology, China, since 2020. He received the B.S. degree in mechanical engineering from Liaoning University of Petroleum and Chemical Technology in 2005, the M.S. degree in mechanical design and theory from Northeastern University, China, in 2008, and the PhD degree in electrical engineering from University College Cork, Ireland, in 2017. His primary research focuses on innovative design and application of compliant mechanisms and robots. He has introduced methods for synthesizing, modeling, and optimizing compliant mechanisms, presented in over 40 peer-reviewed papers. He is serving as an Associate Editor of IEEE Robotics and Automation Letters, and of Mechanical Sciences. He has earned some accolades including the ASME Compliant Mechanism Award in 2022, the ASME SMRDC Award in 2022, the CMETSC Teaching Award in 2022.

Longteng Yi received the B.S. degree in mechanical engineering from Ningbo University, Ningbo, China, in 2022.

He is currently pursuing the M.S. degree in vehicle engineering with the school of Mechanism Engineering at Dalian University of Technology, Dalian, China. His research interests include compliant mechanisms and computer vision.

Chuyang Leng received the B.S. degree in Vehicle Engineering from China University of Petroleum, Qingdao, China, in 2017.

He is currently pursuing the M.S. degree in vehicle engineering with the school of Mechanism Engineering at Dalian University of Technology, Dalian, China. His research interests include compliant mechanisms and mechanism synthesis.

Yahan Zhong received the B.S. degree in automotive service engineering from Chang'an University, Xian, China, in 2019.

She is currently pursuing the M.S. degree in vehicle engineering with the School of Mechanism Engineering at Dalian University of Technology, Dalian, China. Her research interests include compliant mechanisms and smart sensors.

Jiaqi Hong received the B.S. degree in vehicle engineering from the Dalian University of Technology, Dalian, China, in 2019.

She is currently pursuing the M.S. degree in aerospace engineering with the School of Mechanics and Aerospace Engineering at Dalian University of Technology, Dalian, China. Her research interests include computational mechanics and its intersection with advanced smart materials.

Xueguan Song received the B.S. degree in mechanical engineering from the Dalian University of Technology, Dalian, China, in 2004, and the M.S. and Ph.D. degrees in mechanical engineering from Dong-A University, Busan, South Korea, in 2007 and 2010, respectively.

He is currently a Professor in the School of Mechanical Engineering, Dalian University of Technology. He has published more than 200 peer-reviewed papers, two books in various research fields including engineering optimization, numerical modelling and data mining. His research interest includes multidisciplinary design optimization, surrogate modeling, AI and digital twin. Dr. Song received many awards such as the Best Paper Award at LDIA'13 Conference, Best Poster Awards at CSO 2011 and PCO 2010 Conferences, and Honorable Mention Award in the PhD student paper symposium and competition at the 2010 ASME PVP Conference.

Guangbo Hao (Fellow of ASME) is a Professor with the School of Engineering and Architecture at University College Cork (UCC), Ireland. He earned his first PhD from Northeastern University, China, in 2008 and his second PhD from Heriot-Watt University, UK, in 2011.

His research interests focus on design of compliant mechanisms and robotics and their innovative applications such as precision manufacturing, energy harvesting and medical devices. He is serving as the Editor-in-Chief of Mechanical Sciences and an Associate Editor of ASME Journal of Mechanisms and Robotics, of IEEE Robotics and Automation Letters, and of Mechanism and Machine Theory. He has won many accolades including the 2017, 2018 and 2022 ASME Compliant Mechanisms Awards and the 2023 UCC President's Awards for Excellence in Teaching. He has published over 200 peer-reviewed papers.